

## Environmentally Assisted Cracking of Nickel Strip in $\text{LiAlCl}_4/\text{SOCl}_2$

1 February 1996

Prepared by

J. A. WASYNCZUK  
Mechanics and Materials Technology Center  
Technology Operations  
Engineering and Technology Group

M. V. QUINZIO  
Electronics Technology Center  
Technology Operations  
Engineering and Technology Group

and

H. F. BITTNER  
Directorate A  
Orbital Systems Operations  
National Systems Group

Prepared for

SPACE AND MISSILE SYSTEMS CENTER  
AIR FORCE MATERIEL COMMAND  
2430 E. El Segundo Boulevard  
Los Angeles Air Force Base, CA 90245

National Systems Group

APPROVED FOR PUBLIC RELEASE;  
DISTRIBUTION UNLIMITED

DTIC QUALITY INSPECTED 6

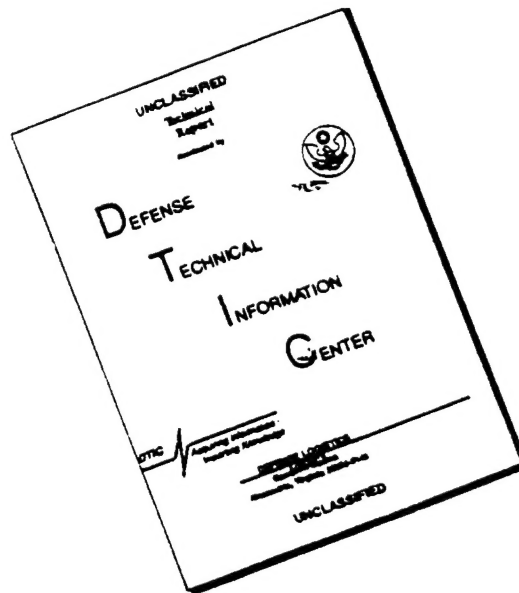
19960325 070



THE AEROSPACE  
CORPORATION

El Segundo, California

# DISCLAIMER NOTICE

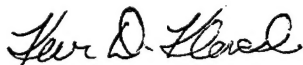


THIS DOCUMENT IS BEST QUALITY AVAILABLE. THE COPY FURNISHED TO DTIC CONTAINED A SIGNIFICANT NUMBER OF PAGES WHICH DO NOT REPRODUCE LEGIBLY.

This report was submitted by The Aerospace Corporation, El Segundo, CA 90245-4691, under Contract No. F04701-93-C-0094 with the Space and Missile Systems Center, 2430 E. El Segundo Blvd., Suite 6037, Los Angeles AFB, CA 90245-4687. It was reviewed and approved for The Aerospace Corporation by T. D. Schoessow, Principal Director, Orbital Systems Operations. Maj. Kevin Klonoski, SMC/CLX, was the project officer.

This report has been reviewed by the Public Affairs Office (PAS) and is releasable to the National Technical Information Service (NTIS). At NTIS, it will be available to the general public, including foreign nationals.

This technical report has been reviewed and is approved for publication. Publication of this report does not constitute Air Force approval of the report's findings or conclusions. It is published only for the exchange and stimulation of ideas.



---

MAJ. KEVIN KLONOSKI  
Project Officer

REPORT DOCUMENTATION PAGE			Form Approved OMB No. 0704-0188	
Public reporting burden for this collection of information is estimated to average 1 hour per response, including the time for reviewing instructions, searching existing data sources, gathering and maintaining the data needed, and completing and reviewing the collection of information. Send comments regarding this burden estimate or any other aspect of this collection of information, including suggestions for reducing this burden to Washington Headquarters Services, Directorate for Information Operations and Reports, 1215 Jefferson Davis Highway, Suite 1204, Arlington, VA 22202-4302, and to the Office of Management and Budget, Paperwork Reduction Project (0704-0188), Washington, DC 20503.				
1. AGENCY USE ONLY (Leave blank)		2. REPORT DATE 1 February 1996		3. REPORT TYPE AND DATES COVERED
4. TITLE AND SUBTITLE  Environmentally Assisted Cracking of Nickel Strip in LiAlCl <sub>4</sub> /SOCl <sub>2</sub>			5. FUNDING NUMBERS  F04701-93-C-0094	
6. AUTHOR(S)  Wasynczuk, James A.; Quinzio, Michael V., and Bittner, Harlan F.				
7. PERFORMING ORGANIZATION NAME(S) AND ADDRESS(ES)  The Aerospace Corporation Technology Operations El Segundo, CA 90245-4691			8. PERFORMING ORGANIZATION REPORT NUMBER  TR-93(3330)-1	
9. SPONSORING/MONITORING AGENCY NAME(S) AND ADDRESS(ES)  Space and Missile Systems Center Air Force Materiel Command 2430 E. El Segundo Blvd. Los Angeles Air Force Base, CA 90245			10. SPONSORING/MONITORING AGENCY REPORT NUMBER  SMC-TR-96-04	
11. SUPPLEMENTARY NOTES				
12a. DISTRIBUTION/AVAILABILITY STATEMENT  Approved for public release; distribution unlimited			12b. DISTRIBUTION CODE	
13. ABSTRACT (Maximum 200 words)  Constant extension rate tests (CERT) were used to evaluate the susceptibility of two cold-rolled nickel strip materials to environmentally assisted cracking (EAC) in 1.5M LiAlCl <sub>4</sub> /SOCl <sub>2</sub> . One strip material was made by a powder metallurgy (PM) process that started with carbonyl nickel. The other was cast and wrought (C&W). Both were 0.05 mm thick and cold-rolled to the three-quarter hard condition. The bulk impurity concentrations, grain structures, and mechanical properties of these two materials were similar. However, the C&W alloy was distinguished by a substantially higher bulk manganese content and oxygen-rich inclusions, a large fraction of which also contained sulfur. EAC of the PM alloy, manifested principally as intergranular fracture, occurred in samples that were polarized to -50, 0, and +200 mV (Li/LiCl), but not in ones that were freely corroding at +3.65 V(Li/LiCl). These results are consistent with EAC being caused by a mechanism involving zero-valent lithium, proposed by Scully <i>et al.</i> In marked contrast to the PM alloys, the C&W alloy exhibited no susceptibility to Li-assisted cracking. In ancillary experiments, performed with samples that were cathodically charged with hydrogen, only the PM alloy exhibited a high susceptibility to intergranular cracking. The present results indicate that subtle microstructural differences may affect the reliability of Li/SOCl <sub>2</sub> cells. Although the existing evidence is circumstantial, the results also suggest that lithium-assisted and hydrogen-assisted intergranular cracking have analogous sensitivities to grain boundary segregation of sulfur.				
14. SUBJECT TERMS  Battery      Nickel Lithium			15. NUMBER OF PAGES  13	
			16. PRICE CODE	
17. SECURITY CLASSIFICATION OF REPORT Unclassified	18. SECURITY CLASSIFICATION OF THIS PAGE Unclassified	19. SECURITY CLASSIFICATION OF ABSTRACT Unclassified	20. LIMITATION OF ABSTRACT	

# Environmentally Assisted Cracking of Nickel Strip in $\text{LiAlCl}_4/\text{SOCl}_2$

J. A. Wasynczuk, M. V. Quinzio, and H. F. Bittner

The Aerospace Corporation, Los Angeles, California 90009-2957, USA

## ABSTRACT

Constant extension rate tests (CERT) were used to evaluate the susceptibility of two cold-rolled nickel strip materials to environmentally assisted cracking (EAC) in  $1.5\text{M LiAlCl}_4/\text{SOCl}_2$ . One strip material was made by a powder metallurgy (PM) process that started with carbonyl nickel. The other was cast and wrought (C&W). Both were 0.05 mm thick and cold-rolled to the three-quarter hard condition. The bulk impurity concentrations, grain structures, and mechanical properties of these two materials were similar. However, the C&W alloy was distinguished by a substantially higher bulk manganese content and oxygen-rich inclusions, a large fraction of which also contained sulfur. EAC of the PM alloy, manifested principally as intergranular fracture, occurred in samples that were polarized to  $-50, 0$ , and  $+200\text{ mV (Li/LiCl)}$ , but not in ones that were freely corroding at  $+3.65\text{ V (Li/LiCl)}$ . These results are consistent with EAC being caused by a mechanism involving zero-valent lithium, proposed by Scully *et al.*<sup>1</sup> In marked contrast to the PM alloy, the C&W alloy exhibited no susceptibility to Li-assisted cracking. In ancillary experiments, performed with samples that were cathodically charged with hydrogen, only the PM alloy exhibited a high susceptibility to intergranular cracking. The present results indicate that subtle microstructural differences may affect the reliability of  $\text{Li}/\text{SOCl}_2$  cells. Although the existing evidence is circumstantial, the results also suggest that lithium-assisted and hydrogen-assisted intergranular cracking have analogous sensitivities to grain boundary segregation of sulfur.

## Introduction

Thionyl chloride ( $\text{SOCl}_2$ ) serves as both a liquid cathode and an electrolyte solvent in high energy density lithium primary cells. Lithium tetrachloroaluminate ( $\text{LiAlCl}_4$ ) is a widely used supporting electrolyte. Good corrosion resistance, weldability, formability, and relatively high electrical and thermal conductivities are some of the attributes that make nickel strip a widely used material for substrates and conductors. Although various cell designs exist, substrates are typically in the form of a mesh, fabricated by expanding or etching strip. Lithium foil is pressed onto anode substrates. Carbon black, which provides a catalyst for the reduction of  $\text{SOCl}_2$ , is applied to cathode substrates. Nickel strip is also commonly used to interconnect substrates to the case of the cell, internal bus-bars, or header feed-throughs. The ability of nickel strip to withstand long-term exposure to  $\text{LiAlCl}_4/\text{SOCl}_2$  solutions is an important factor in cell reliability. Under appropriate conditions, however, environmentally assisted cracking of nickel can pose a reliability hazard.

The susceptibility of nickel to EAC in  $\text{LiAlCl}_4/\text{SOCl}_2$  solutions is critically dependent on potential.<sup>1</sup> Due to the formation of an  $\text{NiCl}_2$  passive film,<sup>2</sup> freely corroding nickel exhibits very low dissolution rates in  $\text{SOCl}_2$  solutions.<sup>2,3</sup> Lithium also forms a passive chloride film in  $\text{SOCl}_2$  solu-

tions.<sup>4</sup> Relative to the  $\text{Li/LiCl}$  equilibrium potential, the corrosion potential of nickel in  $1.5\text{M LiAlCl}_4/\text{SOCl}_2$  has been measured at  $+3.65\text{ V}$ .<sup>2,4</sup> At this potential, nickel is not susceptible to pitting, localized weld-zone corrosion, or EAC.<sup>1,3</sup> Although some polarization occurs during cell discharge, cathode substrates and conductors experience potentials that are not far from  $+3.65\text{ V (Li/LiCl)}$ . Polarization at the lithium anodes is typically less than at the cathodes. Therefore, anode substrates and conductors, being coupled to lithium, are maintained at potentials near  $0\text{ V (Li/LiCl)}$ . A susceptibility to EAC has been demonstrated for nickel that was cathodically polarized to potentials equal, or negative to,  $0\text{ V (Li/LiCl)}$ .<sup>1</sup> Some susceptibility to EAC also was found at  $+200\text{ mV (Li/LiCl)}$ .<sup>1</sup>

The susceptibility of nickel to EAC in  $\text{LiAlCl}_4/\text{SOCl}_2$  was demonstrated by CERT. These slow-strain-rate tensile tests revealed that the ductility of swaged Ni 200 rod was markedly decreased when it was tested at, or negative to, the  $\text{Li/LiCl}$  potential in  $1.5\text{M LiAlCl}_4/\text{SOCl}_2$ .<sup>1</sup> Convincing experimental evidence supported the proposal that the observed ductility reduction was caused by a form of solid metal-induced embrittlement by zero valent lithium.<sup>1</sup> The occurrence of EAC at  $+200\text{ mV (Li/LiCl)}$  is consistent with this explanation if the reasonable possibility of underpotential deposition of lithium is considered.<sup>1</sup> Although the

Table I. Chemical compositions of the two alloys studied.

Alloy designation	Ni	C	Co	Cr	Cu	Fe	Mg	Mn	S	Si	Ti
PM	bal.	0.04	nd	nd	0.02	0.01	nd	0.01	0.001	0.01	nd
C&W	bal.	0.05	0.03	0.01	0.03	0.02	0.01	0.23	0.002	0.05	0.01
UNS N02200	99.0	0.15			0.25	0.40		0.35	0.010	0.35	
Nickel 200 <sup>a</sup>	min	max			max	max		max.	max	max	
UNS N02201	99.0	0.02			0.25	0.40		0.35	0.010	0.35	
Nickel 201 <sup>a</sup>	min	max			max	max		max.	max	max	
UNS N02270	99.97	0.02	0.001	0.001	0.001	0.005	0.001	0.001	0.001	0.001	0.001
Nickel 270 <sup>a</sup>	min	max	max	max	max	max	max	max.	max	max	max

The concentrations of C and S were determined by LECO combustion. Inductively coupled plasma emission spectroscopy was used for all other elements. nd = not determined. The compositions of three common alloys are included for comparison. They are designated by the Unified Numbering System, and their INCO trade names.

exact nature of the mechanism remains uncertain, the findings of high crack growth rates (estimated to be  $>10^{-5}$  mm/s), and the extent of EAC being nearly independent of test temperature and displacement rate, indicated a surface-induced cracking process that involves practically no diffusion of lithium into nickel.<sup>1</sup>

Similarities among various forms of EAC have long been recognized, with sensitivity to grain boundary segregation being one of them.<sup>5,6</sup> For example, antimony and tin increase the susceptibility of high strength steels to hydrogen-assisted cracking (HAC), liquid-metal embrittlement, and temper embrittlement.<sup>5</sup> Literature searches failed to uncover data on the effects of impurities on metal-induced embrittlement of nickel. However, for HAC, the topic has been thoroughly studied. The susceptibility of nickel to intergranular HAC is sensitive to trace levels of sulfur.<sup>7-10</sup> Sulfur has a strong tendency to segregate to grain boundaries in nickel,<sup>8-10</sup> and its deleterious effects have been attributed to a catalytic enhancement of hydrogen uptake, a lowering of grain boundary cohesive strength, and enhancement of plasticity.<sup>7-13</sup> In experiments with zone-refined nickel ( $\leq 4$  wt. ppm S) and Ni 270 ( $\leq 10$  wt. ppm S), grain boundary concentrations of sulfur have been systematically increased from levels undetectable by scanning Auger microscopy to more than 4 atomic percent (a/o), by annealing samples that were initially quenched from a higher solutionizing temperature.<sup>8-10</sup> The results of these experiments demonstrated direct relationships between grain boundary sulfur concentrations and the extent of intergranular HAC.<sup>8-10</sup> However, at high hydrogen fugacities, such as that produced by cathodic charging at  $-1$  V saturated calomel electrodes (SCE) in  $0.1N$   $H_2SO_4$ , even solutionized-and-quenched samples exhibited exclusively intergranular fracture.<sup>10</sup> It is likely that the strong tendency for intergranular HAC in these high-purity nickels is promoted by an absence of inclusions, or other microstructural defects, suitable for the nucleation of transgranular fracture.<sup>12</sup>

HAC of nickel can occur transgranularly, often by quasi-cleavage and/or microvoid coalescence.<sup>1,10-15</sup> Although the mechanistic details of crack nucleation are not well understood, there is evidence that precipitates, inclusions, and defects resulting from cold work, promote transgranular HAC.<sup>10-17</sup> The accumulation of hydrogen at particle/matrix interfaces, or other trapping sites, appears to be central to this behavior.<sup>10-17</sup> Because hydrogen diffuses rapidly in nickel,<sup>18</sup> it can interact with defects well within the bulk of a test specimen when long charging times are employed.<sup>11,12</sup>

Here, CERT was used to evaluate the susceptibility of two nickel strip materials to EAC in  $1.5M$   $LiAlCl_4/SOCl_2$ . CERT has been widely used to evaluate susceptibility to EAC, particularly stress corrosion cracking (SCC).<sup>19,20</sup> Although exceptions exist, it has generally been found that if SCC does not occur in properly controlled CERT, then it does not occur in service.<sup>20</sup> Parallels between EAC in  $LiAlCl_4/SOCl_2$  and HAC were explored by ancillary experiments in which the nickel strips were manually fractured after being cathodically charged with hydrogen in an aqueous  $H_2SO_4$  solution.

## Experimental

Two nickel strip materials were studied. One was made by a PM process that started with carbonyl nickel. The other was C&W. Their chemical compositions are listed in Table I. Except for a substantially higher Mn level in the C&W alloy, the compositions of the two alloys are similar. Manganese was measured at 0.23 weight percent (w/o) for the C&W alloy, but only 0.01 w/o for the PM alloy. The compositions of three common grades of commercially pure nickel, UNS N02200, N02201, and N02270,<sup>21,22</sup> are included in Table I for comparison. Alloys with similar compositions are perhaps more commonly known by the International Nickel Company trade names Ni 200, Ni 201, and Ni 270.<sup>23</sup> Both of the 0.05 mm thick strip materials were obtained in the three-quarter hard cold-rolled condition. Both had high quality surface finishes with finely spaced parallel rolling marks that were visible under oblique lighting. Comparison with reference surfaces indicated a finish similar to that of a ground surface with  $0.2 \mu m$  rms roughness. Metallographic cross sections of the strips were prepared by standard grinding and mechanical polishing methods. An etchant consisting of equal volumes of  $HNO_3$  and  $CH_3COOH$  was used to reveal grain structure. Grain sizes were determined by the linear intercept method. Following the guidelines in American Society for Testing and Materials (ASTM) E 112-84, standard methods for determining average grain size, size determinations were made along parallel line arrays that coincided with the principal directions of the strips. Nonmetallic inclusions in the C&W alloy were revealed by chemically polishing the broad faces of the strip in a heated ( $80^\circ C$ ) solution of 30 ml  $HNO_3$ , 10 ml  $H_2SO_4$ , 10 ml  $H_3PO_4$ , and 50 ml  $CH_3COOH$ .

Two groups of "dog bone" shaped tensile specimens, a subsized version of the geometry described in ASTM specification E 345, were machined from each of the 0.05 mm thick nickel strips. Specimens that were machined such that the tensile axis was parallel to the rolling direction are referred to as longitudinal specimens. Specimens that were machined such that the tensile axis was normal to the rolling direction are referred to as transverse specimens. The transition from a 4.8 mm wide, 22 mm long, reduced section to 9 mm wide grip sections was made by 16 mm radius fillets. To facilitate loading by pinned connections, the grip sections of each dog bone were spot-welded to  $1.5 \times 9 \times 32$  mm type 316-L stainless steel tabs. Although stress concentrations and localized softening of the nickel strip were natural consequences of these spot-welds, the effects were small enough to allow nearly all our specimens to fail in the reduced section. Tensile properties were determined from tests that were performed in air, on a screw-driven Instron machine, operated at a  $2.1 \times 10^{-3}$  mm/s crosshead displacement rate. For the 22 mm reduced section, this displacement rate gave an engineering strain rate of  $9.5 \times 10^{-4} s^{-1}$ . To intentionally create a concentration of tensile stress that would promote the initiation of EAC, a 1.3 mm diam circular hole was electric-discharge machined into the center of the reduced section of some specimens.

A simplified schematic diagram of the hermetic cell in which the specimens were tested is shown in Fig. 1. Tensile loads were transmitted to the specimen through a bottom-cap that was attached to the crosshead of the CERT load frame, and a plug that was attached to the load cell. The plug and the bottom-cap were made from type 316-L stainless steel. Macor® (a trademark of Dow-Corning) machinable ceramic spacers insulated the specimen from the loading pins. A bolted o-ring seal joined the bottom-cap to a cylindrical containment tube. A sliding o-ring seal allowed axial movement between the plug and the containment tube. The containment tube in our prototype test cell was made of Teflon® (a trademark of Du Pont). Although this Teflon tube performed its containment function well, repeated assembly and disassembly caused excessive wear of tapped bolt-holes. Two additional cells, both with type 316-L stainless steel tubes, were therefore constructed. Viton® (a trademark of Du Pont) o-rings were used for static seals like the one that joined the bottom-cap to the containment tube. Although it is well known that Viton is not stable in  $\text{SOCl}_2$ , data from previous experiments indicated that it would perform adequately for at least 48 h. In nearly all our tests, Viton was also used in the sliding o-ring seal. Exposure to electrolyte vapor caused the Viton to swell, and this impeded movement of the plug. However, we found no evidence that this compromised the hermeticity of the cell. For example, the response of the nickel strips did not change when replicate tests were performed with a Kalrez® (a trademark of Du Pont) o-ring in the sliding seal. The manufacturer reports that Kalrez perfluoroelastomer is stable in  $\text{SOCl}_2$ .

Assembly of the test cell was facilitated by a special fixture (not shown in Fig. 1) that both shielded the specimen from inadvertent compressive and torsional loads, and insured that the specimen was electrically insulated from the tube and the reference/counterelectrode. This special fixture, made of type 316-L stainless steel and Macor ceramic, also served to reduce the volume of electrolyte needed to fill the cell. Roughly 6 ml of electrolyte filled the cell to the upper pinned connection, with most of this volume surrounding the reduced section of the specimen and the reference/counterelectrode. The reference/counterelectrode consisted of an  $\sim 0.38 \times 10 \times 15$  mm strip of lithium

foil that was pressed onto a piece of 0.25 mm thick nickel mesh. A perforated ceramic compartment in the special fixture held a broad face of this electrode approximately 3 mm away from a broad face of the specimen's reduced section. Nickel wires were used to connect the specimen and the mesh that supported the reference/counterelectrode to hermetic feed-throughs in the plug. Spot-welds were used to make these wired interconnections.

Assembly of the test cell, and filling it with electrolyte, were performed in a glove box with a dry ( $<35$  ppm moisture) argon atmosphere. The specimen and all parts of the test cell, except the o-rings, were oven-dried at  $90^\circ\text{C}$  for at least 12 h prior to assembly. The electrolyte was a battery grade  $1.5\text{M LiAlCl}_4/\text{SOCl}_2$  that was purchased from the Lithium Corporation of America, Gastonia, NC. The 0.38 mm thick battery grade (99.8%) lithium foil also was purchased from the Lithium Corporation of America. Immediately after assembly and filling, the hermetic test cell was transferred from the glove box to the CERT apparatus, which was in air.

Except for tests in which the nickel specimen was freely corroding at approximately  $+3.65$  V (Li/LiCl), the potential of the specimen was controlled by a potentiostat (EG&G Princeton Applied Research Model 363). Potentials were applied within 10 min from the time that the test cell was filled with electrolyte. Prior to the application of potentiostatic control, cathodic polarization of the specimen was achieved by a small ( $\sim 0.5 \times 5 \times 10$  mm) strip of lithium foil that was pressed onto a piece of nickel mesh that was spot-welded to the lower grip section. This was done to approximate the polarization of anode substrates and conductors in actual Li/SOCl<sub>2</sub> cells, which are in contact with lithium at the time they are filled.

Because the results from CERT of swaged Ni 200 rod indicate that embrittlement is more severe at  $-50$  mV than at  $0$  V (Li/LiCl),<sup>1</sup> most of our tests were performed at  $-50$  mV (Li/LiCl). Transverse specimens of the PM alloy were also tested at  $0$ ,  $+0.2$ , and  $+3.65$  V (Li/LiCl). Our standard procedure was to begin straining the specimen after it had been maintained at the test potential for  $\sim 17$  h. This  $\sim 17$  h holding period was initially employed to facilitate characterization of the ionic currents in the test cell. When specimens that had been fractured at  $0$  and  $-50$  mV (Li/LiCl) were removed from the cell, lithium dendrites were found on their reduced sections. Dendrites were observed on the edges and both broad faces of the reduced sections, with the greatest depositions usually found on the broad face adjacent to the reference/counterelectrode. These observations convinced us that the test cell allowed ample exposure of the reduced sections to lithium in the electrolyte. In subsequent tests, the procedure of holding the specimen at the test potential for roughly 17 h prior to straining was maintained for consistency.

The loading apparatus used for CERT was a modification of a unit that was designed and built in-house, for previous projects. Its crosshead was driven by a stepper motor, with gearing that gave it the capacity to pull a 500 N load. As is commonly found in tensile testing,<sup>24</sup> compliance of the grips and testing machine caused the slope of the linear-elastic portion of our load-displacement curves to be substantially less than an estimate based on the dimensions of the thin strip specimens and the elastic modulus of nickel (207 GPa).<sup>23</sup> Measured slopes deviated from this estimated value by roughly a factor of four for tests performed with the Instron machine to roughly a factor of eight for tests performed with the CERT loading apparatus (test cell filled with water). All CERT were performed at a crosshead displacement rate of  $7.5 \times 10^{-5}$  mm/s. For the 22 mm reduced section, this displacement rate gave an engineering strain rate of  $3 \times 10^{-6}$  s<sup>-1</sup>, which falls within the range of strain rates used for CERT of swaged Ni 200 rod.<sup>1</sup> Problems with the digital control of the stepper motor foiled attempts to perform CERT at lower strain rates. Upon completion of each CERT, the test cell was disassembled in a fume hood, in air.

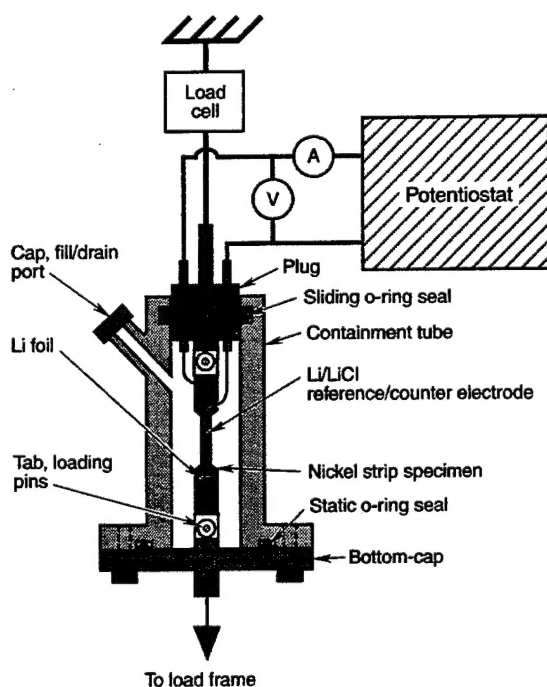


Fig. 1. Schematic diagram of the CERT apparatus.

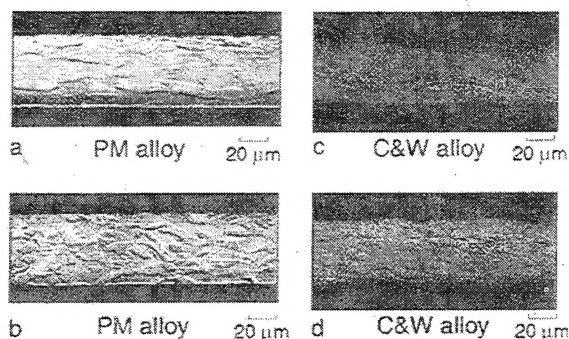


Fig. 2. Optical micrographs of polished and etched cross sections of the nickel strips. In (a) and (c), the rolling direction is parallel to the length of the micrograph. In (b) and (d), the rolling direction is normal to the plane of the page.

The susceptibility of the nickel strip to HAC was evaluated by manually bending cathodically charged specimens to tight radii. Strips measuring  $4.8 \times 38$  mm were charged for 24 h at  $-1$  V (SCE) in  $1N$   $H_2SO_4$ . Arsenic trioxide (500 mg/liter) was used to poison the hydrogen recombination reaction.<sup>9</sup> It has been shown that charging at  $-1$  V (SCE) in  $1N$   $H_2SO_4$  is more than sufficient to cause HAC in susceptible nickel alloys.<sup>1,8-12</sup> Assuming that the penetration of hydrogen scales with  $\sqrt{D_H t}$  where  $D_H$  is the lattice diffusion coefficient for hydrogen in nickel ( $\sim 4 \times 10^{-10}$  cm<sup>2</sup> s<sup>-1</sup>,<sup>18</sup>) and  $t$  is the 24 h charging period, a diffusion distance on the order of 0.06 mm is obtained. Since this calculated diffusion distance exceeds the 0.025 mm half-thickness, and grain boundaries may have increased diffusion rates, it is reasonable to assume that the present procedure allowed hydrogen to permeate the entire specimen.

After cathodic charging, the specimens were thoroughly rinsed in deionized water, dried, and then bent until fracture was observed. Transverse specimens of the PM and C&W alloys, one each, were examined subsequently by Auger electron spectroscopy (AES). AES was performed with a VG Scientific LTD ESCALAB MK II, operated such that a 5 keV electron beam irradiated an area measuring roughly  $30 \times 30$  μm. Five different areas were analyzed for each specimen. A constant retard ratio of 4 was selected on the 150° spherical sector electron energy analyzer. The analysis depth is estimated to be 50 to 100 Å. Surface compositions were calculated from element peak-to-peak amplitudes of first derivative spectra, using the equation<sup>25</sup>

$$C_x = (I_x/S_x) / \sum_i I_i/S_i$$

where  $C_x$  is the atomic concentration of element  $x$ ,  $I_x$  and  $I_i$  are the peak-to-peak amplitudes of elements  $x$  and  $i$ , respectively, and  $S_x$  and  $S_i$  are the relative sensitivities of elements  $x$  and  $i$ , respectively. The following sensitivity factors were used: 0.27 for Ni (847 eV), 0.40 for C, 0.13 for O, and 0.73 for S. Because AES was preceded by roughly 2 days storage in laboratory air, it was recognized that atmospheric contamination would interfere with chemical analysis of the native fracture surfaces.

### Results

Cold-rolling to the three-quarter hard condition created anisotropy in the grain structure of the nickel strips. Elongation of the grains in the rolling direction is revealed in the optical micrographs shown in Fig. 2. The size and shape of the grains in both alloys were similar. For both the PM and C&W alloys, average grain dimensions were  $\sim 20$  μm in the longitudinal (rolling) direction, 8 μm in the long-transverse direction, and 5 μm in the short-transverse (through thickness) direction.

Optical and scanning electron microscopic (SEM) examination of the cross sections indicated that the principal microstructural difference between the C&W and PM alloys was nonmetallic inclusions, which were found in the

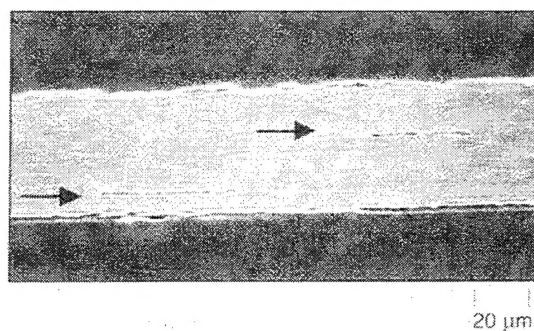


Fig. 3. SEM image of a mechanically polished cross section of the C&W alloy. The rolling direction is parallel to the length of the micrograph. Two elongated pits, formed by pullout of stringer inclusions, are marked with arrows.

C&W alloy, but not the PM alloy. Mechanical polishing caused pullout of most of these inclusions. However, the resulting pits revealed that they were typically in the form of stringers, roughly 1–3 μm diam and 10–50 μm long. Most of these stringer inclusions were located within the center three-quarters of the strip. An example is shown in Fig. 3. Consistent with them being confined to the interior of the strip, these stringer inclusions were not revealed by SEM examination of the rolled surfaces of the as-received material. Inclusions suitable for windowless energy-dispersive x-ray spectroscopy (EDXS) were revealed by chemically polishing the broad faces of the C&W strip. Several inclusions were examined. They were all rich in Mg and O. Most of them also contained readily detectable amounts of S. Some also contained detectable amounts of Al, Ti, Ca, and Mn. Because of their strong tendencies to form oxide, sulfide, and oxysulfide precipitates, additions of Mg, Ca, Mn, or rare-earth elements, are used to control O and S in melt-processed Ni-rich alloys.<sup>26</sup> Thorough examination of cross sections revealed that the PM alloy was practically free of nonmetallic inclusions.

The results of the tensile tests are summarized in Table II. Each value represents the average from at least three tests. For each alloy and specimen type, the measured values of strength differed from the mean by  $<5\%$ . Examples of the load-displacement curves that were used to generate these data are shown in Fig. 4. The axes of this graph are labeled as engineering stress and engineering strain, defined as crosshead displacement/reduced-section length. The data in Table II indicate that cold-rolling imparted little anisotropy to the tensile properties of the nickel strips. For both alloys, transverse specimens tended to exhibit ultimate tensile strengths that were 3 to 6% greater than those of the longitudinal specimens. Averaging both specimen types, the ultimate tensile strength of the C&W alloy exceeded that of the PM alloy by roughly 5%.

In thin strip specimens that are tested to failure under uniaxial tension, large plastic strains are typically confined to narrow regions of localized necking in which the thickness rapidly decreases to fracture.<sup>27-29</sup> Because the axial displacements associated with such localized necks were small relative to the 22 mm long reduced section, the present specimens exhibited very low values of elongation-to-failure. Values on the order of 0.4% were obtained from

Table II. Tensile properties.

Alloy	Specimen type	Proportional limit (MPa)	Ultimate tensile strength (MPa)	Reduction of area (%)
PM	longitudinal	559	608	98
PM	transverse	554	629	98
C&W	longitudinal	573	631	97
C&W	transverse	567	671	97

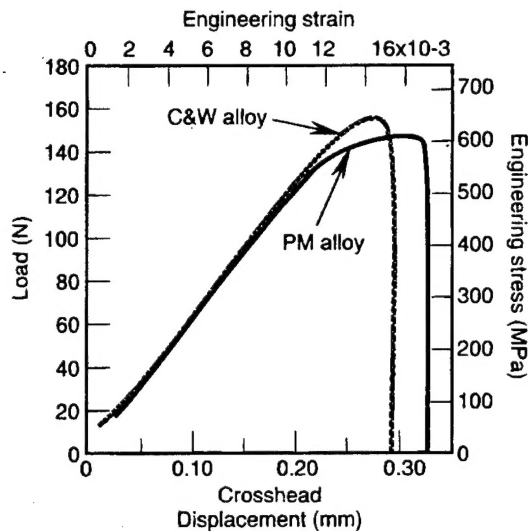


Fig. 4. Tensile load-displacement curves for longitudinal specimens of the PM and C&W alloys, tested in air, on an Instron machine.

engineering stress-strain curves. The stress representing the onset of macroscopic plastic deformation is therefore reported in Table II as the proportional limit (the stress at which the engineering stress-strain curve became nonlinear), rather than the more common 0.2% offset yield stress. Tensile ductility is reported as the reduction of area,  $RA = (A_0 - A_f)/A_0$ , where  $A_0$  is the cross-sectional area of the original gage section, and  $A_f$  is the projected area of the fracture surface. Both alloys exhibited high ductility. Values of  $RA$  approaching 100% mean that the thin strip specimens necked down to what looked like a chisel with isolated segments of microvoid coalescence along its edge. An example is shown in Fig. 5. This type of tensile fracture surface was found in the longitudinal and the transverse specimens of both alloys.

Localized necks tend to traverse a specimen's width along relatively straight lines that are inclined to the tensile axis.<sup>27,28</sup> In both the longitudinal and the transverse specimens of both alloys, localized necks tended to form along lines that were inclined from the tensile axis by 56 to 59°. A photograph illustrating fracture at a localized neck is shown in Fig. 6a. Our measured values of 56 to 59° are not far from the 54.7° that is predicted for localized neck formation along lines of zero normal strain in an isotropic plastic-rigid sheet.<sup>27,28</sup> In the presence of a notch, however, localized necking can be induced along lines that are approximately normal to the tensile axis.<sup>28</sup> For example, the

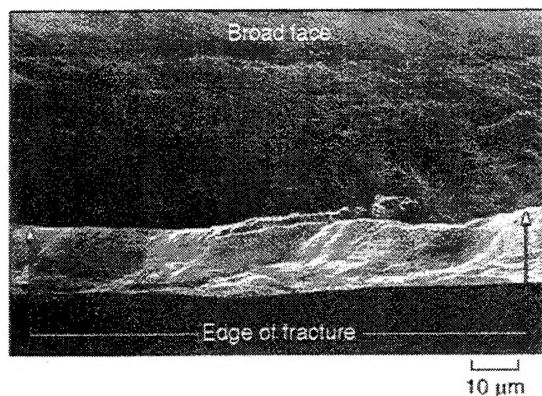


Fig. 5. An SEM image of a fracture surface produced by tensile testing in air. A longitudinal specimen of the PM alloy is shown.

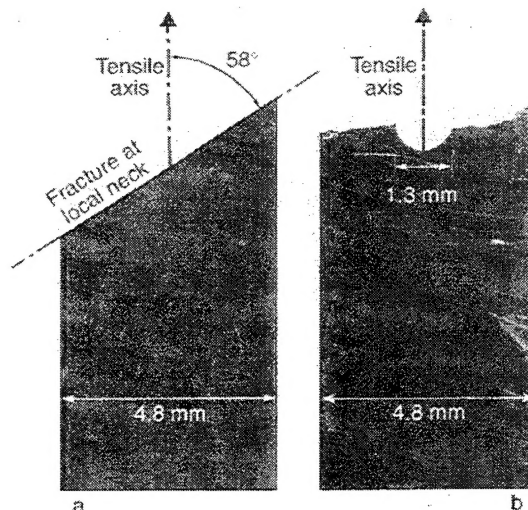


Fig. 6. Photographs illustrating typical macroscopic fracture paths for tensile tests performed in air. (a) A transverse specimen and (b) a notched longitudinal specimen of the PM alloy are shown.

1.3 mm diam circular hole that was electric-discharge machined into the center of the reduced section of some of our tensile specimens caused localized necking and subsequent chisel-edge fracture to initiate at the edges of the hole, and then propagate approximately normal to the tensile axis. This sequence of deformation and fracture was ascertained by video-imaging tensile tests that were performed on the CERT loading apparatus. These video images clearly showed that an extensive period of slow localized necking at the edges of the hole preceded final fracture, which occurred by rapid ductile crack growth. A photograph of a notched specimen that was tested to failure in air is shown in Fig. 6b.

A total of 21 CERT were performed. The number of tests performed for each combination of alloy, specimen type, and test potential are listed in Table III. Our principal finding was that CERT at -50 mV (Li/LiCl) produced EAC in both the transverse and the longitudinal specimens of the PM alloy, but not at all in the C&W alloy. EAC was manifested in load-displacement curves, macroscopic fracture paths, and microscopic fracture surface appearance.

The most revealing indicator of EAC was intergranular fracture. SEM images illustrating intergranular fracture in transverse and longitudinal specimens of the PM alloy are shown in Fig. 7 and 8, respectively. Particularly for the transverse specimen, we can see that there is little reduction of area associated with the intergranular regions. Careful SEM examination of specimen reduced sections indicated that secondary cracks were practically nonexistent in regions removed from the fracture surface. Secondary intergranular cracks, like those marked with arrows in Fig. 8, were observed only within the localized necks. SEM fractography also revealed slip lines on intergranular facets. Similar features have been reported for intergranular HAC of nickel.<sup>13</sup> It is uncertain if the present slip lines were produced during CERT or prior cold-rolling.

Table III. A listing of the number of CERT that were performed.

Alloy, specimen type	Test potential (Li/LiCl)			
	-50 mV	0 V	+200 mV	+3.65 V
PM, transverse	5	4	1	2
PM, longitudinal	3			
C&W, transverse	1			
C&W, longitudinal	2			
PM, notched transverse	1			
PM, notched longitudinal	1			
C&W, notched longitudinal	1			

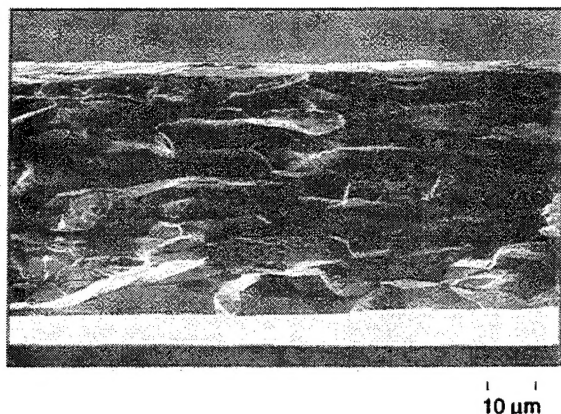


Fig. 7. SEM image of an intergranular fracture surface of a transverse specimen of the PM alloy, produced by CERT at  $-50$  mV (Li/LiCl).

In marked contrast to the PM alloy, CERT at  $-50$  mV (Li/LiCl) produced only chisel-edge fracture surfaces in both the transverse and the longitudinal specimens of the C&W alloy. These exclusively chisel-edge fracture surfaces were similar to those produced by tensile testing in air. Careful SEM examination of fractured specimens revealed practically no evidence of intergranular or cleavage cracking in the C&W alloy.

As a comparison of Fig. 7 and 8 indicates, longitudinal specimens of the PM alloy were more resistant to intergranular EAC than transverse specimens. In each longitudinal specimen, CERT at  $-50$  mV (Li/LiCl) produced two or more separate regions of intergranular fracture, always originating at an edge or broad face, but rarely extended more than half-way through the thickness. The large remainder of each specimen always exhibited chisel-edge fracture surfaces. From SEM examinations, in which the fracture surface was viewed parallel to the tensile axis, it was estimated that the total projected area of these intergranular regions amounted to only about 3 to 6% of the original  $0.05 \times 4.8$  mm cross-sectional area. Although considerably more prominent than in the longitudinal specimens, intergranular EAC in the transverse specimens of the PM alloy was also limited in extent. Regions of intergranular fracture produced by CERT at  $-50$  mV (Li/LiCl) usually traversed the entire thickness of the transverse specimens, but they were usually confined to one or two, 0.5 to 1.5 mm long, segments of the approximately 4.8 mm long width. In

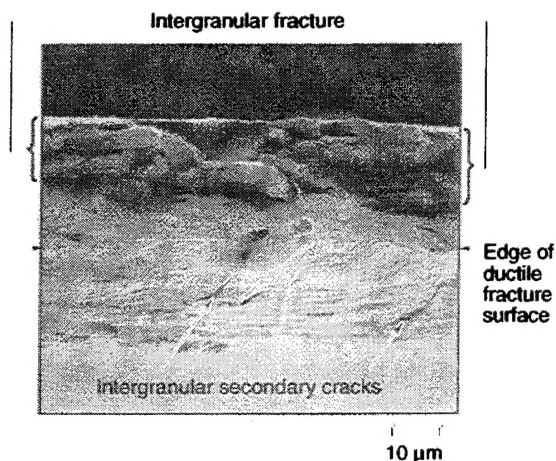


Fig. 8. SEM image of a mixed intergranular and chisel-edge fracture surface of a longitudinal specimen of the PM alloy, produced by CERT at  $-50$  mV (Li/LiCl).

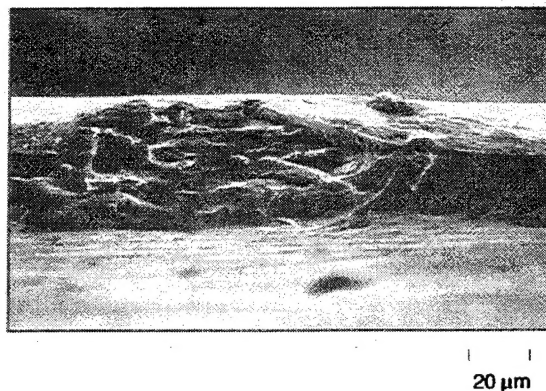


Fig. 9. SEM image showing a transition from an intergranular to a chisel-edge fracture surface in a transverse specimen of the PM alloy, produced by CERT at  $-50$  mV (Li/LiCl).

each specimen, the total projected area of these intergranular regions typically amounted to roughly 5 to 30% of the original cross-sectional area. The remaining segments always displayed chisel-edge fracture surfaces. An SEM image illustrating a transition from intergranular to chisel-edge fracture in a transverse specimen is shown in Fig. 9.

The occurrence of EAC was manifested also in macroscopic fracture paths. Specimens that exhibited intergranular EAC tended to fracture along paths that were approximately normal to the tensile axis. Specimens that did not exhibit EAC fractured along paths that were inclined to the tensile axis, practically the same as the fracture paths produced by tensile tests in air. Examples are shown in Fig. 10.

The load-displacement curves generated during CERT provided another useful indicator of EAC. However, the interpretation of these data was complicated by the non-ideal behavior of the sliding o-ring seal. Observations made during post-CERT cell disassemblies indicated that exposure to electrolyte vapor increased the force required to move the plug within its containment tube, especially for a Viton o-ring in a stainless steel containment tube. We attribute much of this behavior to swelling of the Viton. Swelling was evidenced by increases in o-ring diameter, which were readily observable after cell disassemblies. Analysis of the load-displacement data indicated that much of the increased force associated with o-ring swelling displayed the characteristics of a relatively constant friction load, defined as the residual load that persisted after specimen failure. Subtraction of this constant friction load from the measured load gives what we term a corrected load that provides a self-consistent parameter for data

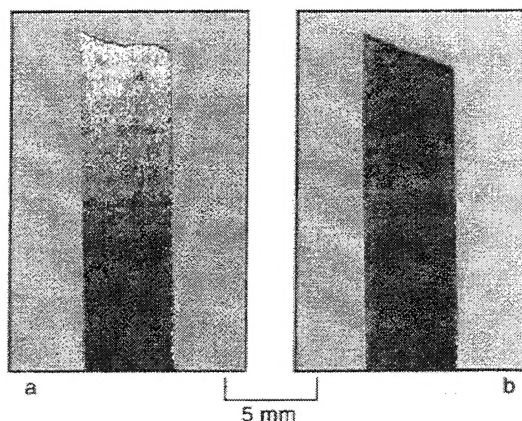


Fig. 10. Photographs illustrating typical macroscopic fracture paths for CERT at  $-50$  mV (Li/LiCl). Longitudinal specimens of the (a) PM and (b) C&W alloys are shown.

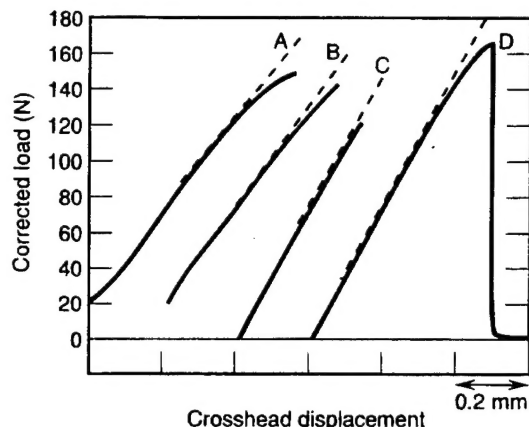


Fig. 11. Representative corrected load-displacement curves: (A) a transverse specimen of the PM alloy tested in water; (B) a longitudinal specimen of the PM alloy tested at  $-50$  mV (Li/LiCl), (C) a transverse specimen of the PM alloy at  $-50$  mV (Li/LiCl), and (D) a transverse specimen of the C&W alloy tested at  $-50$  mV (Li/LiCl). Annotation with straight lines highlights displacement beyond the proportional limit.

comparison. The larger friction loads found for the stainless steel containment tubes are attributed to them being substantially stiffer, and built to closer tolerances, than the prototype Teflon tube. When a Kalrez o-ring was used to seal a stainless steel containment tube, the magnitude of the friction load was reduced.

Representative corrected load-displacement curves for the PM and C&W alloys are shown in Fig. 11. The three curves to the left are for the PM alloy. For curve D, the rapid drop in load associated with specimen failure, and the subsequent residual friction load (21 N in this case), are included. A comparison of curves A-C reveals that the susceptibility of the PM alloy to EAC is manifested by reductions in the maximum corrected load and an attendant loss of displacement beyond the proportional limit. Since the C&W alloy did not exhibit EAC, the load-displacement curves obtained by CERT at  $-50$  mV (Li/LiCl) had the same shape as those obtained by tensile testing in air.

The PM alloy's much higher susceptibility to EAC at  $-50$  mV (Li/LiCl) was reinforced by the results of CERT of the three specimens that contained a 1.5 mm diam circular notch. The stress concentration associated with the notch promoted intergranular fracture of the PM alloy. For both the transverse and the longitudinal specimen, intergranular fracture initiated at both sides of the notch, where maximum tensile stresses are expected. In the transverse specimen, intergranular fracture extended for as much as 2 mm from the surface of the notch, always traversing the entire specimen thickness. Intergranular fracture also traversed the entire thickness of the notched longitudinal specimen, extending for as much as 0.8 mm from the surface of the notch. Beyond these intergranular regions, all the notched specimens of the PM alloy exhibited chisel-edge fracture surfaces. In marked contrast to the PM alloy CERT at  $-50$  mV (Li/LiCl) did not produce any intergranular fracture, or other brittle fracture modes, in the notched longitudinal specimen of the C&W alloy. Fracture of this specimen remained ductile, similar to that produced by tensile tests in air.

To ascertain that the observed EAC was caused by a mechanism involving zero-valent lithium, transverse specimens of the PM alloy were also tested at 0, +0.2, and +3.65 V (Li/LiCl). The load-displacement curves, macroscopic fracture paths, and fracture surfaces produced by CERT at 0 V were similar to those produced by CERT at  $-50$  mV (Li/LiCl). Intergranular EAC was also produced by CERT at +200 mV (Li/LiCl). However, the regions of intergranular fracture produced at this potential were

smaller than those at 0 and  $-50$  mV, and they often did not traverse the entire thickness of the specimen. CERT at +3.65 V (Li/LiCl) did not produce any EAC in the transverse specimens of the PM alloy. Instead, the fracture surfaces were exclusively chisel-edge, with macroscopic fracture paths similar to those produced by tensile testing in air. The corrected load-displacement curves produced by CERT at +3.65 V (Li/LiCl) were similar to those produced when the test cell was filled with water (curve A in Fig. 11).

Hydrogen charging greatly reduced the ductility of both alloys. In the as-received condition, the PM and C&W strips could be bent to tight radii without cracking. After the 24 h charging period, transverse specimens of both alloys fractured when they were bent to a radius of roughly 0.15 mm. SEM examinations revealed that HAC of the PM alloy was exclusively intergranular, and slip lines were observed on the intergranular facets. For the C&W alloy, HAC occurred by a roughly equal mixture of microvoid coalescence and transgranular quasi-cleavage. Regions of intergranular fracture were seldom observed. A typical fracture surface for the C&W alloy is shown in Fig. 12. SEM examination of the fracture surface shown in Fig. 12 did not give obvious indications that transgranular HAC was nucleated by decohesion of the large stringer inclusions seen in the cross sections.

As was expected for samples that were fractured and stored in laboratory air, the Auger spectra obtained from the hydrogen-charged samples contained large carbon and oxygen peaks. Because of these peaks, and other uncertainties associated with atmospheric contamination, the present data do not provide an accurate measure of native fracture surface composition. However, they do suggest that the average grain boundary concentration of sulfur in the PM alloy is not unusually high. For both the PM and the C&W alloy specimens, only nickel, oxygen, carbon, and sulfur were detected on the fracture surfaces. Also for both specimens, sulfur was not detected on the broad faces that were exposed to the electrolyte. For the intergranular fracture surface of the PM alloy, measurable amounts of sulfur were detected in only two of the five  $30 \times 30$   $\mu\text{m}$  areas analyzed. For the predominantly transgranular fracture surface of the C&W alloy, at least trace amounts of sulfur were detected in all five areas analyzed. The average fracture surface compositions were nearly the same for both alloys, approximately 53 Ni/15 O/32C/ $\leq 1$ S (a/o). The compositions of the most sulfur-rich areas also were similar for both alloys, approximately 58 Ni/11 O/29C/2S.

## Discussion

The present finding of intergranular EAC in the PM alloy following CERT at  $-50$ , 0, and +200 mV (Li/LiCl), but not at +3.65 (Li/LiCl), parallels the results reported by Scully

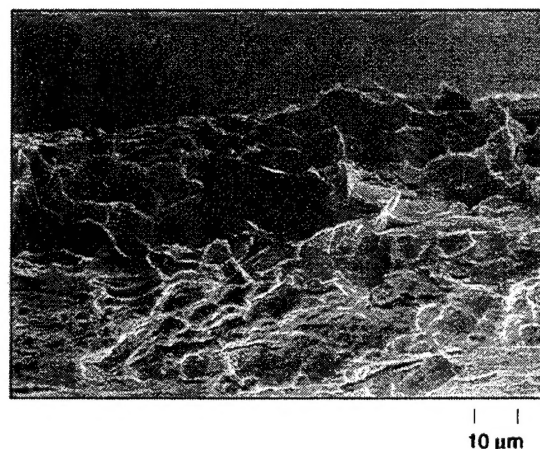


Fig. 12. SEM image of a fracture surface of a transverse specimen of the C&W alloy produced by bending after hydrogen charging.

*et al.* for CERT of swaged Ni 200 rod.<sup>1</sup> This marked effect of potential, as well as other experimental results from their study, strongly supported their proposal that the observed EAC was a form of solid metal-induced embrittlement by zero-valent lithium. The occurrence of EAC at +200 mV (Li/LiCl) is consistent with this explanation if the reasonable possibility of underpotential deposition of lithium is considered.<sup>1</sup> As described by Scully *et al.*, the observed effect of potential is not consistent with HAC. HAC was discounted primarily because all likely hydrogen evolution reactions are not uniquely related to the Li/LiCl equilibrium potential. Specifically, candidate reactions for the formation of H<sup>•</sup> by the dissociation of trace amounts of water in LiAlCl<sub>4</sub>/SOCl<sub>2</sub> are independent of potential, and the formation of H by the reduction of H<sup>•</sup> is likely to occur at a potential that is considerably more positive than 0 V (Li/LiCl).<sup>1</sup> Although the present study did not include a battery of ancillary CERT to eliminate the possibility of HAC systematically, the observed effect of potential provides a strong indication that intergranular fracture of the PM alloy during CERT at -50, 0, and +200 mV (Li/LiCl) was also caused by a mechanism involving zero-valent lithium.

The susceptibility of the PM alloy to Li-assisted intergranular cracking was clearly demonstrated by the results of CERT at -50 mV (Li/LiCl). However, in both the transverse and the longitudinal specimens, CERT produced limited amounts of intergranular fracture. In the transverse specimens, the projected area of intergranular regions amounted to 5 to 30% of the original cross section. In the longitudinal specimens, intergranular fracture was confined to regions near the exposed surfaces, and they amounted to only 3 to 6% of the original cross section. The greater resistance to Li-assisted cracking implied by these fractographic data is corroborated by the corrected load-displacement curves for the PM alloy (compare curves B and C in Fig. 11), which illustrate the substantially larger displacement beyond the proportional limit exhibited by longitudinal specimens. It is likely that the more tortuous intergranular crack path provided by the longitudinal specimens played a large role in this enhanced resistance to Li-assisted cracking. Analogous grain orientation effects have been reported for HAC of cold-rolled nickel.<sup>11</sup>

The projected area fraction of brittle fracture produced by CERT is a parameter that is often used to quantify the susceptibility to EAC. When susceptible materials are tested in aggressive environments, it is not unusual for values of this parameter to approach, or equal, 100%.<sup>1,7-14</sup> Although CERT at -50 mV (Li/LiCl) produced comparatively low area fractions of intergranular fracture in the PM alloy, the fractographic and load-displacement data indicate that this does not reflect a moderate susceptibility to Li-assisted cracking, particularly for the transverse specimens. Rather, these data indicate that the comparatively small amounts of intergranular fracture were a consequence of its termination by ductile fracture that occurred so rapidly, it outpaced Li-assisted cracking.

Evidence that intergranular cracking preceded ductile fracture is found in the SEM images that show that there was little reduction of area associated with intergranular fracture of both the transverse and the longitudinal specimens of the PM alloy (Fig. 7-9). This sequence of fracture processes is supported by the changes in macroscopic fracture path that accompanied Li-assisted cracking. Analogous to the effect of the circular hole on tensile fracture in air (Fig. 6), regions of intergranular fracture produced during CERT acted as notches, causing subsequent localized necking and ductile fracture to occur along lines approximately normal to the tensile axis (Fig. 10). The absence of secondary cracks in regions removed from the fracture surface indicates that intergranular cracking started at loads close to the breaking load, and that the first intergranular region to form usually grew to become the flaw that induced final ductile fracture. The results of video-imaging tensile tests of notched specimens provided clear evidence that final ductile fracture was very rapid. Since the axial displace-

ments associated with tensile failure of the thin strip specimens were small, it is likely that rapid final fracture was promoted by a quick release of elastic strain energy that was stored in the specimen and the relatively compliant CERT loading apparatus. More extensive EAC might be produced by performing CERT at lower displacement rates on a stiffer load frame, or by changing to a specimen geometry that promotes stable crack growth.

CERT at -50 mV (Li/LiCl) produced only ductile fracture in both the transverse and the longitudinal specimens of the C&W alloy. Since the tensile strength of this alloy was only about 5% greater than that of the PM alloy, it is unlikely that the quick release of elastic strain energy that limited the extent of intergranular fracture in the PM alloy could have completely suppressed Li-assisted cracking in the C&W alloy. An inherent resistance to Li-assisted cracking is strongly supported by the finding that CERT at -50 mV (Li/LiCl) also failed to produce any brittle fracture in the notched longitudinal specimen of the C&W alloy. The results of video-imaging tensile tests clearly showed that rapid final fracture of this type of specimen is preceded by an extensive period of slow plastic deformation in the vicinity of the circular notch. This slow plastic deformation, and the concomitant high tensile stresses, should have provided ample opportunity for the occurrence of Li-assisted cracking at -50 mV (Li/LiCl).

Given the similarities in bulk chemical composition, grain structure, and tensile properties, it is remarkable that the two nickel strip materials displayed such different susceptibilities to Li-assisted cracking. Likely reasons for this behavior can be inferred from the results of the HAC experiments, metallography, and the extensive literature on HAC of nickel and nickel-based alloys. Although the evidence is circumstantial, the indication is that Li-assisted and H-assisted intergranular cracking of nickel have analogous sensitivities to grain boundary segregation of sulfur.

As with Li-assisted cracking, HAC of the PM alloy was exclusively intergranular. Although HAC of nickel can occur transgranularly,<sup>10-14</sup> exclusively intergranular HAC is a characteristic that is common to cathodically charged high-purity nickel, such as Ni 270 and zone-refined Ni.<sup>7-12</sup> It is well known that this fracture mode is promoted by grain boundary segregation of sulfur.<sup>8-11</sup> However, under the severe hydrogen charging conditions employed in our experiments, intergranular fracture can occur in the absence of readily measurable segregation.<sup>8-11</sup> The present Auger data, which suggest that the average grain boundary concentration of sulfur in the PM alloy was less than approximately 1 a/o, are consistent with this behavior. Given the absence of readily measurable grain boundary segregation, it seems likely that the strong tendency for exclusively intergranular EAC in the PM alloy was also promoted by the absence of inclusions, or other microstructural defects, suitable for the nucleation of transgranular fracture.<sup>12,16</sup>

The C&W alloy exhibited no signs of Li-assisted cracking, but hydrogen-charged samples fractured by a roughly equal mixture of quasi-cleavage and microvoid coalescence. The microstructural features responsible for this strong tendency for transgranular HAC have not been ascertained. However, since relatively large plastic strains, and stresses well above the proportional limit, are typically associated with microvoid coalescence, the abundance of this ductile fracture mode provides a strong indication that intergranular HAC does not occur easily in the C&W alloy. Given the well-established influence of grain boundary chemistry on intergranular fracture, it is reasonable to assume that this resistance to intergranular HAC is related to low levels of intergranular sulfur, or perhaps other cosegregation effects.<sup>8-10</sup> Since the results of EDXS indicate that the nonmetallic inclusions in the C&W alloy tend to contain sulfur, it is likely that their gettering action lowered the amount of sulfur free to segregate to grain boundaries. Evidence for this mechanism has been described in reports on the high temperature ductility of nickel-based superalloys.<sup>26</sup> The high manganese content of the C&W alloy also may have contributed to its resistance to intergranular

HAC. Although the mechanism is uncertain,<sup>18</sup> experimental data clearly indicate that Mn and Mg reduce the susceptibility of nickel to intergranular HAC.<sup>13</sup>

The exact reasons why the C&W alloy exhibited transgranular EAC after hydrogen charging, but not during CERT at -50 mV (Li/LiCl), are not certain. Although one interpretation of these results is that zero-valent Li was not as effective as H in promoting transgranular fracture, the finding that Li-assisted cracking of swaged Ni 200 rod was primarily by quasi-cleavage does not support this view.<sup>1</sup> Instead, it appears that the behavior of the C&W alloy highlights the differences between embrittlement due to hydrogen that permeated the entire specimen, relative to zero-valent lithium, which was most probably confined to the exposed surfaces. Although the results of our ancillary experiments leave mechanisms uncertain, a large body of data indicate that the interaction of solute hydrogen with microstructural defects was central to transgranular crack nucleation.<sup>11,12,14-17</sup> It follows that the absence of transgranular EAC during CERT at -50 mV (Li/LiCl) may have been a consequence of the exclusion of zero-valent lithium from potent crack nuclei. The low solubility of lithium in nickel, and a diffusivity that is most probably much lower than that of hydrogen, are likely reasons for this exclusion.

The present CERT results have clearly demonstrated that subtle differences in microstructure can have large effects on the susceptibility of nickel strip to Li-assisted cracking. More recent work, performed on the same PM alloy used in this study, has shown that a susceptibility to Li-assisted cracking also can be manifested in constant-strain (static-bend) tests that may more closely approximate conditions in actual Li/SOCl<sub>2</sub> cells.<sup>30</sup> However, the occurrence of cracking in these specimens was critically dependent on subtle differences in polarization and the resulting surface layers of LiCl.<sup>30</sup> It is therefore apparent that specification of the exact microstructural and electrochemical conditions likely to cause Li-assisted cracking of nickel in Li/SOCl<sub>2</sub> cells requires additional study. Given the extensive body of data on HAC of nickel, it appears that the Ni-Li/SOCl<sub>2</sub> system may offer unique opportunities for research on the similarities of different types of EAC.

### Conclusions

Constant extension rate tests (CERT) were used to evaluate the susceptibility of two cold-rolled nickel strip materials to environmentally assisted cracking (EAC) in 1.5M LiAlCl<sub>4</sub>/SOCl<sub>2</sub>. One strip material was made by a powder metallurgy (PM) process that started with carbonyl nickel. The other was cast and wrought (C&W). The bulk impurity concentrations, grain structures, and mechanical properties of these two materials were similar. However, the C&W alloy was distinguished by a substantially higher bulk manganese content and oxygen-rich inclusions, a large fraction of which also contained sulfur. EAC of the PM alloy occurred in samples that were polarized to -50, 0, and +200 mV (Li/LiCl), but not in ones that were freely corroding at +3.65 V (Li/LiCl). These results are consistent with EAC being caused by a mechanism involving zero-valent lithium, proposed by Scully *et al.* Li-assisted cracking of the PM alloy was exclusively intergranular. Its extent was limited by the onset of rapid ductile fracture, promoted by the combined effects of a compliant load frame and the small failure strains that are characteristic of thin strip specimens. In marked contrast to the PM alloy, the C&W alloy exhibited no susceptibility to Li-assisted cracking. In ancillary experiments, performed with cathodically charged specimens, the C&W alloy was resistant to intergranular hydrogen-assisted cracking. The present results indicate that subtle microstructural differences may affect the reliability of Li/SOCl<sub>2</sub> cells. Although the existing evidence is circumstantial, the results also suggest that lithium-assisted and hydrogen-assisted intergranular cracking have analogous sensitivities to grain boundary segregation of sulfur.

### Acknowledgment

AES was performed by C. Hemminger. The assistance of T. Barrera, R. Brose, S. Frost, G. Henderson, C. Hoover, J. Marcus, B. Nelson, F. Ross, C. Su, and J. Uht is greatly appreciated. Helpful discussions with B. Carter and L. Thaller, of Aerospace, as well as W. Cieslak, and others at SANDIA, are greatly appreciated also.

Manuscript submitted Oct. 3, 1994; revised manuscript received May 1, 1995. This was in part Paper 114 presented at the New Orleans, LA, Meeting of the Society, Oct. 10-15, 1993.

The Aerospace Corporation assisted in meeting the publication costs of this article.

### REFERENCES

1. J. R. Scully, W. R. Cieslak, F. S. Bovard, *This Journal*, **138**, 2229 (1991).
2. W. R. Cieslak, F. M. Delnick, D. E. Peebles, and J. W. Rogers, Jr., in *Surfaces, Inhibition, and Passivation*, E. McCafferty and R. J. Brodd, Editors, PV 86-7, p. 368, The Electrochemical Society Proceedings Series, Pennington, NJ (1986).
3. R. C. McDonald and K. M. Lechiaro, *This Journal*, **135**, 1313 (1988).
4. E. Peled, in *Lithium Batteries*, Jean-Paul Gabano, Editor, p. 43, Academic Press, New York (1983).
5. N. S. Stoloff, in *Environment-Sensitive Fracture of Engineering Materials*, Z. A. Foroulis, Editor, p. 486, The Metallurgical Society of AIME, Warrendale, PA (1979).
6. S. P. Lynch, *Acta Metall.*, **36**, 2639 (1988).
7. R. M. Latanision and H. Opperhauser, Jr., *Metall. Trans.*, **5**, 483 (1975).
8. S. M. Bruemmer, R. H. Jones, M. T. Thomas, and D. R. Baer, *Metall. Trans. A*, **14A**, 223 (1983).
9. R. H. Jones, S. M. Bruemmer, M. T. Thomas, and D. R. Baer, *ibid.*, **14A**, 1729 (1983).
10. T. S. F. Lee and R. M. Latanision, *ibid.*, **18A**, 1653 (1987).
11. D. Verpoort, D. J. Duquette, N. S. Stoloff, and A. Neu, *Mater. Sci. Eng.*, **64**, 135 (1984).
12. S. Ashok, D. J. Duquette, N. S. Stoloff, and C. Verpoort, *Scr. Met.*, **15**, 1329 (1981).
13. J. Eastman, T. Matsumoto, N. Narita, F. Heubaum, and H. K. Birnbaum, in *Hydrogen Effects in Metals*, I. M. Bernstein and A. W. Thompson, Editors, p. 397, The Metallurgical Society of AIME, Warrendale, PA (1981).
14. R. E. Stoltz and A. J. West, *ibid.*, p. 541.
15. M. W. Joosten, T. D. Lee, T. Goldenberg, and J. P. Hirth, *ibid.*, p. 839.
16. A. W. Thompson and I. M. Bernstein, *ibid.*, p. 291.
17. H. Cialone and R. J. Asaro, *ibid.*, p. 767.
18. G. J. Thomas, *ibid.*, p. 77.
19. *Stress Corrosion Cracking—The Slow Strain-Rate Technique*, ASTM STP 665, G. M. Ugiansky and J. H. Payer, Editors, ASTM, Philadelphia, PA (1979).
20. J. A. Beavers and G. H. Koch, *Corrosion*, **48**, 256 (1992).
21. *Metals and Alloys in the Unified Numbering System*, 3rd ed., p. 175, Society of Automotive Engineers, Warrendale, PA (1983).
22. ASTM Standard Specification for Nickel Plate, Sheet, and Strip, B 162-80.
23. Product Data Sheets, Huntington Alloy Products Division, International Nickel Co., Huntington 17, WV.
24. P. P. Gillis and T. S. Gross, in *Metals Handbook*, Vol. 8, 9th ed., p. 38, ASM, Metals Park, OH (1985).
25. *Handbook of Auger Electron Spectroscopy*, 2nd ed., Physical Electronics Industries, Inc., Eden Prairie, MN (1976).
26. F. Cosandey and J. Kandra, *Metall. Trans. A*, **18A**, 1239 (1987).
27. W. A. Backofen, *Metall. Trans.*, **4**, 2679 (1973).
28. R. Hill, *J. Mechanics and Physics of Solids*, **1**, 19 (1952).
29. E. B. Kula and N. H. Fahey, *Materials Research and Standards*, **1**, 631 (1961).
30. W. R. Cieslak, D. E. Weigand, and R. G. Buchheit, Abstract 113, p. 191, The Electrochemical Society Extended Abstracts, Vol. 93-2, New Orleans, LA, Oct. 10-15, 1993.

## TECHNOLOGY OPERATIONS

The Aerospace Corporation functions as an "architect-engineer" for national security programs, specializing in advanced military space systems. The Corporation's Technology Operations supports the effective and timely development and operation of national security systems through scientific research and the application of advanced technology. Vital to the success of the Corporation is the technical staff's wide-ranging expertise and its ability to stay abreast of new technological developments and program support issues associated with rapidly evolving space systems. Contributing capabilities are provided by these individual Technology Centers:

**Electronics Technology Center:** Microelectronics, VLSI reliability, failure analysis, solid-state device physics, compound semiconductors, radiation effects, infrared and CCD detector devices, Micro-Electro-Mechanical Systems (MEMS), and data storage and display technologies; lasers and electro-optics, solid state laser design, micro-optics, optical communications, and fiber optic sensors; atomic frequency standards, applied laser spectroscopy, laser chemistry, atmospheric propagation and beam control, LIDAR/LADAR remote sensing; solar cell and array testing and evaluation, battery electrochemistry, battery testing and evaluation.

**Mechanics and Materials Technology Center:** Evaluation and characterization of new materials: metals, alloys, ceramics, polymers and composites; development and analysis of advanced materials processing and deposition techniques; nondestructive evaluation, component failure analysis and reliability; fracture mechanics and stress corrosion; analysis and evaluation of materials at cryogenic and elevated temperatures; launch vehicle fluid mechanics, heat transfer and flight dynamics; aerothermodynamics; chemical and electric propulsion; environmental chemistry; combustion processes; spacecraft structural mechanics, space environment effects on materials, hardening and vulnerability assessment; contamination, thermal and structural control; lubrication and surface phenomena; microengineering technology and microinstrument development.

**Space and Environment Technology Center:** Magnetospheric, auroral and cosmic ray physics, wave-particle interactions, magnetospheric plasma waves; atmospheric and ionospheric physics, density and composition of the upper atmosphere, remote sensing using atmospheric radiation; solar physics, infrared astronomy, infrared signature analysis; effects of solar activity, magnetic storms and nuclear explosions on the earth's atmosphere, ionosphere and magnetosphere; effects of electromagnetic and particulate radiations on space systems; space instrumentation; propellant chemistry, chemical dynamics, environmental chemistry, trace detection; atmospheric chemical reactions, atmospheric optics, light scattering, state-specific chemical reactions and radiative signatures of missile plumes, and sensor out-of-field-of-view rejection.